Article

Sr₂TiO₄ Prepared Using Mechanochemical Activation: Influence of the Initial Compounds' Nature on Formation, Structural and Catalytic Properties in Oxidative Coupling of Methane

Svetlana Pavlova, Yulia Ivanova, Sergey Tsybulya, Yurii Chesalov, Anna Nartova [ID]**, Evgenii Suprun and Lyubov Isupova *** [ID]

Boreskov Institute of Catalysis, pr. Lavrentieva, 5, 630090 Novosibirsk, Russia
* Correspondence: isupova@catalysis.ru

Abstract: Methane oxidative coupling (OCM) is considered a potential direct route to produce C_2 hydrocarbons. Layered perovskite-like Sr_2TiO_4 is a promising OCM catalyst. Mechanochemical activation (MA) is known to be an environmentally friendly method for perovskite synthesis. Sr_2TiO_4 were synthesized using MA of the mixtures containing $SrCO_3$ or SrO and TiO_2 or $TiO(OH)_2$ and annealing at 900 and 1100 °C. XRD and FT-IRS showed that MA leads to the starting component disordering and formation of $SrTiO_3$ only for SrO being pronounced when using $TiO(OH)_2$. After annealing at 900 °C, Sr_2TiO_4 was mainly produced from the mixtures of $SrCO_3$ or SrO and $TiO(OH)_2$. The single-phase Sr_2TiO_4 was only obtained from MA products containing $SrCO_3$ after calcination at 1100 °C. The surface enrichment with Sr was observed by XPS for all samples annealed at 1100 °C depending on the MA product composition. The OCM activity of the samples correlated with the surface Sr concentration and the ratio of the surface oxygen amount in SrO and perovskite (O_o/O_p). The maximal CH_4 conversion and C_2 yield (25.6 and 15.5% at 900 °C, respectively), and the high long-term stability were observed for the sample obtained from ($SrCO_3$ + TiO_2), showing the specific surface morphology and optimal values of the surface Sr concentration and O_o/O_p ratio.

Keywords: layered strontium titanates; mechnochemical activation; methane oxidative coupling

1. Introduction

With large fossil resources of natural and shale gas, gas hydrates promote the development of processes for methane conversion into valuable chemicals. Among them, the direct catalytic conversion of methane to C_2 hydrocarbons by oxidative coupling (OCM) is considered a potential route for processing methane into useful products [1–3]. Researchers generally agree that a simplified heterogeneous–homogeneous mechanism of OCM occurs via the activation of methane to methyl radicals on the catalyst surface, the subsequent homogeneous coupling of two methyl radicals to ethane in the gas phase and oxidative dehydrogenation of ethane to ethylene. In parallel, nonselective (homogeneous and/or heterogeneous) oxidation can proceed to give COx. The reaction complexity hinders the development of efficient OCM catalysts [1–3]. On the whole, OCM activity of the catalysts is ensured by oxygen activation creating the active sites for generation of methyl radicals and high basicity for fast desorption of methyl radicals that could be tuned by catalyst composition [1–4]. Although many studies devoted to OCM have been performed and various catalytic materials have been investigated for this reaction, commercial implementation of OCM has not yet been reached, since the C_2 yield is relatively low [1,5–7]. Thus, design of the stable OCM catalysts with a high methane conversion rate and C_2 selectivity remains a relevant problem.

A number of previous studies revealed that some perovskite-type oxides containing alkaline, alkaline-earth and rare-earth elements exhibit certain activity and C_2 selectivity

for the OCM reaction [1,8–19]. Perovskites have high thermal and chemical stability, while concentration of surface defects, active oxygen species and basic sites can be tailored by adjusting their chemical composition. Along with chemical composition, the surface and bulk properties could be affected by the perovskite crystalline structure. All these properties make perovskites promising catalysts for OCM. Among them, much attention has been paid to titanate and stannate perovskite catalysts based on regular ABO_3 [9–16] and layered Ruddlesden–Popper $A_{n+1}B_nO_{3n+1}$ [17–19] structures (A = Ca, Ba, Sr, B = Ti, Sn). The perovskite-like Ruddlesden–Popper-type oxides are comprised of alternating layers of ABO_3 perovskite and AO rock salt and exibit high oxygen mobility due to the peculiarities of its fine structure [10,20,21]. It was found in an earlier report by Yang et al. [17] that the layered Sr_2TiO_4 and Sr_2SnO_4 perovskites demonstrated better performance in OCM at 800 °C than the corresponding $SrTiO_3$ and $SnTiO_3$. Recently, it was shown that the fine crystal structure of different strontium stannates influences their OCM performance, which follows in the order of $Sr_2SnO_4 > Sr_3Sn_2O_7 > SrSnO_3$ [10]. The results of multiple methods reveal that the coordination environment of Sr cations is altered depending on perovskite type, making the formation of surface oxygen vacancies easier for Sr_2SnO_4 than for $Sr_3Sn_2O_7$ and $SrSnO_3$. This explains why Sr_2SnO_4 has the largest quantities of active surface oxygen and basic sites, as well as the best OCM performance.

The high OCM activity and selectivity of doped Sr_2TiO_4 (C_2 yield up to 25% and C_2 selectivity around 66% at 850–900 °C) were found in [18] and related to the segregation of SrO on the catalyst surface under the reaction conditions. SrO increases the basicity of the surface and lowers the amount of weakly adsorbed molecular oxygen species that can shift the reaction to the deep oxidation. The effect of Sr surface enrichment resulting from the surface reconstruction of the model $SrTiO_3$ on OCM activity was studied in [14]. CH_4 conversion, C_2 selectivity and the ratio of C_2H_4/C_2H_6 was found to increase at the Sr enrichment of the surface up to Sr/(Sr + Ti) of 0.66 and then levels off. Thus, the results evidence that the optimal surface concentration of Sr could promote the high OCM activity of the catalysts based on strontium titanates.

It is known that the presence of certain active oxygen species and basic sites determining the high catalytic performance of perovskite-type oxides in methane oxidative reactions are strongly influenced by preparation method and synthesis parameters, such as the nature of the raw chemicals, pH and temperature, etc. [1–3]. Along with the optimal surface properties, the effective OCM catalysts could have a low specific surface area (SSA) to prevent unselective homogeneous reactions [1–3]. Different methods can be used for synthesis of titanates, including: solid state reaction [11–13,15,17], spray and glycine-nitrate combustion [10,11], hydrothermal synthesis [15], coprecipitation [15,19], the polymer precursor method [16,22], the sol-gel method [19,23] and mechanochemical activation [18,19,24–26]. Fu et al. [11] investigated Ca, Sr, Ba titanates prepared by solid-state and spray combustion methods for the OCM reaction. They found that the samples prepared by the solid-state method, being of lower crystallinity, showed the better OCM performance due to the high surface concentration of alkaline earth metal cations, which is beneficial for C_2 formation. The study of $SrTiO_3$ samples synthesized using a solid-state reaction, molten salt and sol-precipitation hydrothermal treatment also shows that the surface atomic structure of perovskite determined by the morphology of crystalline nanoparticles depends on the synthesis method used [15]. The dependence of the texture and morphology of Sr_2TiO_4 prepared via the ultrasonic modified sol-gel method on the alkaline agent adjusting the pH was shown in [21]. It was shown in [19] that the phase composition of the OCM catalysts based on Sr_2TiO_4, their texture features (specific surface area, pore size and volume) and the distribution of active surface oxygen species depends on the synthesis method: co-precipitation, sol precipitation, citrate or mechanochemical activation (MA) methods with further calcinations at 1100 °C. The catalysts prepared by sol precipitation and MA were the most effective for OCM, giving a C_2 yield of about 12% at 800–900 °C. Doped Sr_2TiO_4 possessing high OCM activity and selectivity were also prepared using MA of the mixtures containing TiO_2, oxides and carbonates in [18].

Usually, the sintered complex oxides with a low SSA are prepared by a solid-state method which requires prolonged heating at high temperatures with the intermediate homogenization of the powder precursors yielding phases with nonuniform particle size distribution and variations in the stoichiometry [11–13,15,17]. So called "wet" methods, such as coprecipitation, the sol-gel method, spray combustion, etc., involve several steps which take many hours to achieve the formation of the target mixed oxide phase and require the use of various chemicals or special complex equipment. Mechanochemical activation (MA) of starting compounds through high energy milling is the alternative route to avoid these problems and it is an environmentally friendly method due to the absence of any wastes [25–30]. During the milling processes, the homogeneity of the mixture increases, the particle size decreases and the new contacts arise. A high-energy input into the reaction zone leads to localized heating and high pressure, resulting in disordering of the crystal structure and the generation of various types of defects in solids that increase their reactivity [29].

In the course of milling, the raw compounds can be transformed into precursors or directly into the target products, depending on their nature and synthesis conditions. The MA effect on the formation of strontium titanates was studied in the early report of Berbenni et al. [25]. The physical mixtures containing $SrCO_3$ and TiO_2 (rutile) (at a ratio of $SrCO_3:TiO_2$ = 1:1, 1:2, 3:2) were dry milled for 110–240 h, depending on their composition. $SrTiO_3$ and Sr_2TiO_4 were not formed during milling and were obtained only after the annealing of the activated mixtures at 800–850 °C for 12 h. MA was applied to obtain Ruddlesden–Popper titanates $Sr_2[Sr_{n-1}Ti_nO_{3n+1}]$ (n = 1–4) in [26]. Stoichiometric mixtures of SrO and TiO_2 (anatase) were activated in a planetary mill for 35–300 h. During MA, $SrTiO_3$ was formed after 35–150 h for all mixtures, except the two $SrO:TiO_2$ compositions. The kinetic study revealed that traces of Sr_2TiO_4 are observed at 70 h; increasing milling time up to 125 h results in the formation of the very low crystallinity Sr_2TiO_4 phase that is transformed into $SrTiO_3$ during further milling. After annealing of the corresponding MA products at 800–1200 °C, the single crystalline phases were only obtained for $SrTiO_3$, Sr_2TiO_4 and $Sr_3Ti_2O_7$. However, the study showed that MA of the initial mixtures leads to the substantial temperature decrease in the synthesis of all members of the layered $Sr_2[Sr_{n-1}Ti_nO_{3n+1}]$ series. It is noted in the paper that this is a result of the grains fracture and defects generated during grinding, which leads to a higher internal energy and reduces the thermal barrier for any subsequent reaction [26].

Thus, the analysis of the previous data shows that perovskite-type layered Sr_2TiO_4 are perspective catalysts for the OCM reaction due to peculiarities of its structure that provide for the large quantities of active surface oxygen and basic sites formed as a result of SrO segregation on the surface. Synthesis of Sr_2TiO_4 with mechnochemical activation is a prospective environmentally friendly method. However, systematic studies on the influence of the raw chemicals' nature on Sr_2TiO_4 synthesis using MA are absent in the literature. In this work, the interaction of raw compounds during MA in the high-energy planetary ball mill, the impact of MA product peculiarities on phase and surface composition, morphology and microstructure of Sr_2TiO_4 layered perovskite obtained after annealing and its catalytic activity in the OCM reaction are studied.

2. Results and Discussion

2.1. Study of MA Products by XRD and FT-IRS

The influence of the starting compounds nature on their interaction and phase composition of the samples after MA has been studied by XRD and FT-IR spectroscopy.

XRD data for the samples after mechanical activation are presented in Figure 1. The patterns of both MA-1 ($SrCO_3$ + TiO_2) and MA-2 ($SrCO_3$ + $TiO(OH)_2$) show the reflections of the starting $SrCO_3$ [PDF 05–418], in addition to the reflections of TiO_2 (rutile) [PDF 21-276] for MA-1. $TiO(OH)_2$ is an amorphous compound. The reflections of starting SrO [PDF 06-0520] and TiO_2 are presented in the pattern of MA-3 (SrO + TiO_2). For MA-4 (SrO + $TiO(OH)_2$), along with the reflections of SrO, a number of the wide peaks in the regions of

2θ~25–29° and 36–40° are observed that could evidence the presence of a minor admixture of strontium carbonate and hydroxide. In addition, the reflections of $SrTiO_3$ [PDF 35-0734] appear for MA-3 and MA-4. In the case of MA-4, their intensity is slightly higher, which could be due to some stronger interaction of SrO with $TiO(OH)_2$ compared to TiO_2.
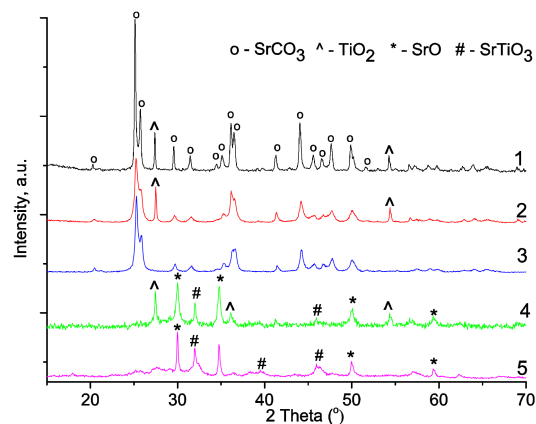

Figure 1. XRD patterns of the physical mixture ($SrCO_3$ + TiO_2) (1) and MA products. MA-1 (2), MA-2 (3), MA-3 (4), MA-4 (5).

The FT-IR spectroscopy data give additional information about the influence of the starting compounds' nature on their interaction during MA and the phase composition of MA products. The FT-IR spectra of the initial TiO_2, $TiO(OH)_2$, $SrCO_3$, SrO, and products of MA are presented in Figures 2–4. The wide absorption band (a.b.) at ~3470 cm^{-1} and a.b. at 1640 cm^{-1} in the spectrum of TiO_2 (Figure 2) could be accordingly assigned to the stretching and bending vibrations of physically absorbed H_2O or its hydroxyl groups [31,32]. The bands in the range of 1250–1050 cm^{-1} are related to the bending vibrations of Ti-OH, while the a.b. in the range of 950–350 cm^{-1} are the characteristic peaks of skeletal stretching and bending vibrations of Ti-O bonds in TiO_2 [32]. The spectrum of $TiO(OH)_2$ shows practically the same absorption bands as TiO_2 but the peaks related to H_2O and OH groups are noticeably higher in intensity [33,34]. Furthermore, two low-intensity a.b. at 1120 and 1050 cm^{-1} related to SO_4^{2-} [35] are observed (Figure 5), which stems from the synthesis method of $TiO(OH)_2$ using $TiOSO_4$ hydrolysis.
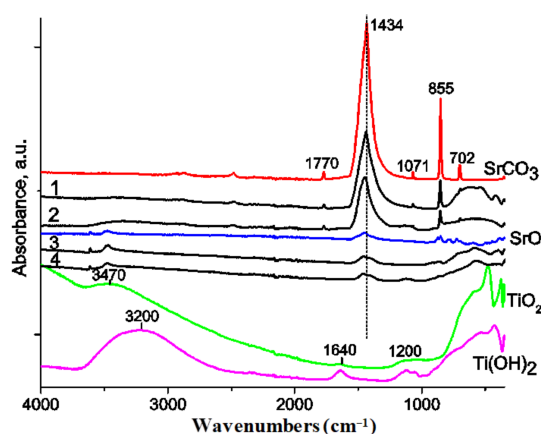

Figure 2. FT-IR spectra of the initial compounds and MA products after mechanical activation for 10 min. 1—MA-1, 2—MA-2, 3—MA-3, 4—MA-4.
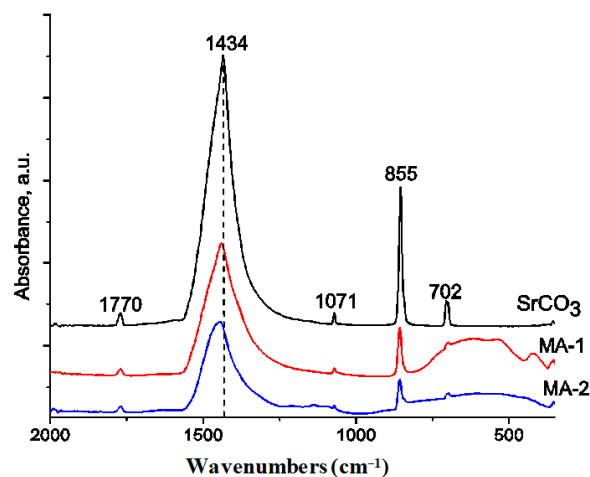
Figure 3. FT-IR spectra (fragment) of the initial $SrCO_3$, MA-1 and MA-2 after mechanical activation for 10 min.
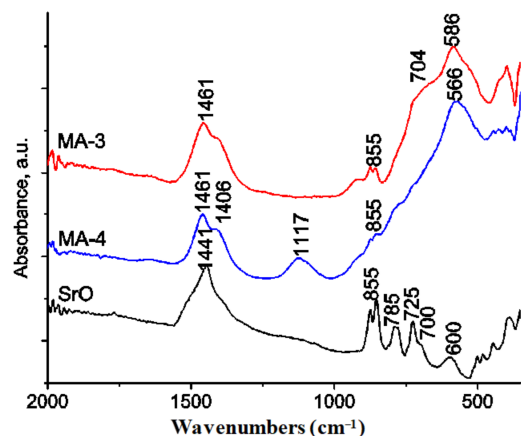

Figure 4. FT-IR spectra (fragment) of the initial SrO, MA-3 and MA-4 after mechanical activation for 10 min.
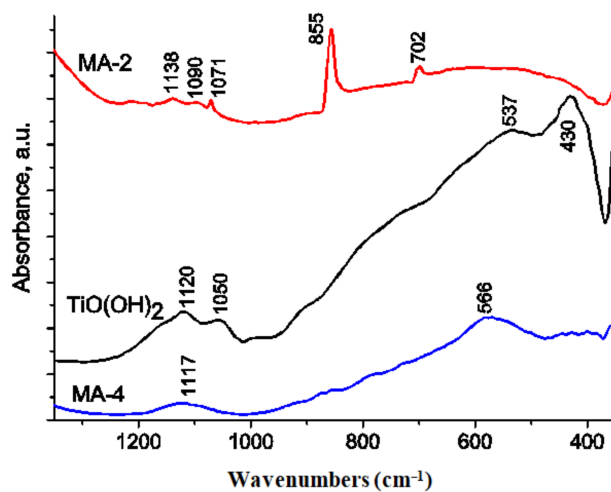

Figure 5. FT-IR spectra (fragment) of MA-2 and MA-4.

The spectrum of the initial $SrCO_3$ shows absorption peaks at 1770, 1434, 1071, 855, 704 and 702 cm^{-1} (Figures 2 and 3). The absorption band at 1770 cm^{-1} is assigned to the bond stretching vibration of C=O in CO_3^{2-} [36]. The intensive a.b. at 1434 cm^{-1} and the weak

a.b. at 1071 cm^{-1} are related to asymmetric and symmetric stretching vibration of C-O band in carbonate anion, while the a.b. at 855, 704 and 699 cm^{-1} can be attributed to the bending out-of-plane and in-plane vibrations [36–38]. After activation in the spectra of the MA-1 (SrCO$_3$ + TiO$_2$) and MA-2 (SrCO$_3$+ TiO(OH)$_2$) samples (Figure 2), the bands of SrCO$_3$ and the wide a.b. at 850–350 cm^{-1} assigned to the characteristic vibrations of Ti-O are observed. For the MA-2 sample, the wide a.b. of the low intensity at 3400 cm^{-1} and 1200–1100 cm^{-1} attributed to vibrations of H$_2$O and OH groups in TiO(OH)$_2$ (Figure 2) are presented as well. Thus, in accordance with the XRD data, FT-IR spectra confirm the presence of the initial compounds in the MA products. However, the bands of SrCO$_3$, TiO$_2$ and TiO(OH) become wider and they are shifted compared with the starting compounds, which evidences the disordering of their crystal structure during MA. All alterations are more pronounced in the spectrum of MA-2, especially for the absorption bands corresponding to the vibrations of the H$_2$O and OH groups in TiO(OH)$_2$ at 3470 cm^{-1}, 1640 cm^{-1} and 1250–1050 cm^{-1} (Figure 2).

In the spectrum of the initial SrO a.b. at 3616 and 3472 cm^{-1} related to the stretching vibrations of OH groups, a.b. at 785 cm^{-1} and 725 cm^{-1} attributed to the bending vibrations of the Sr-OH bond and the bands at 1445 cm^{-1}, 850 cm^{-1} and 705 cm^{-1} assigned to SrCO$_3$ are observed (Figures 2 and 4). The high frequency of the bands corresponding to the OH group's stretching vibrations and their small width evidence the presence of strontium hydroxide [39,40]. Thus, the low intensity of the corresponding absorption bands implies that a small impurity of strontium carbonate and hydroxide presents in SrO, although the starting SrO was obtained shortly before the synthesis. This is explained by its high ability to hydration and carboxylation when exposed to atmospheric CO$_2$ and H$_2$O at room temperature and standard pressure [26]. The band at 600 cm^{-1} and the bands at 550–350 cm^{-1} correspond to the skeletal stretching and bending vibrations of Sr-O [39,40]. The spectra of the activated MA-3 (SrO + TiO$_2$) and MA-4 (SrO + TiO(OH)$_2$) samples are mainly similar (Figures 2 and 4). They show the bands at 3616 and 3472 cm^{-1} corresponding to the vibrations of OH groups, the bands at 1460 cm^{-1} and 900–705 cm^{-1} assigned to SrCO$_3$ and a pronounced a.b. at ~560–586 cm^{-1}, along with the bands in the range of 500–350 cm^{-1} that characterize the stretching and bending vibrations of Me (Sr, Ti)-O bonds. Furthermore, the bands shift and the substantial decrease in the intensity of a.b. characterizing the starting TiO$_2$ and TiO(OH)$_2$ (Figure 2) are observed, which could be a result of their disordering and interaction with SrO. Thus, the pronounced band at ~560–586 cm^{-1} assigned to the vibrations of TiO$_6$ octahedron [41,42] evidences the formation of SrTiO$_3$ in accordance with XRD data (Figure 1). The bands of SrCO$_3$ at 900–705 cm^{-1} are presented in the spectrum of MA-3, while they are absent in the case of MA-4 (Figure 4). This indicates a less effective interaction of SrO with TiO$_2$ compared to TiO(OH)$_2$ during MA, as the XRD data show (Figure 1).

Therefore, the XRD and FT-IRS data for MA products demonstrate that, during mechanical treatment, SrCO$_3$ possesses a lower reactivity compared with SrO, and only the disordering of the starting components is observed in the mixtures containing SrCO$_3$ (MA-1 and MA-2). Low SrCO$_3$ reactivity was also found in [25] when strontium titanates were not formed during prolonged milling of SrCO$_3$ + TiO$_2$ (rutile) mixture using a high-energy planetary mill at 400 rpm rotation. In the case of SrO-containing mixtures (MA-3 and MA-4), along with disordering of the starting components, formation of SrTiO$_3$ is observed in MA products. The formation of traces and the very low crystallinity Sr$_2$TiO$_4$ after milling of the 2SrO + TiO$_2$ mixture in the planetary mill at 200 rpm rotation speed for 70 and 125 h, correspondingly, were demonstrated by Hungrıa et al. [26]. In so doing, they did not observe the formation of intermediate SrTiO$_3$, in contrast with our results (Figures 1 and 4). Such a difference could be because a very-high power planetary ball mill at a 800 rpm rotation rate and acceleration of 40 g was used in our work. The high-energy input in the reaction zone results in the more effective dispersing and mixing of the components [43], as well as their disordering, which increases the number of contact sites and components reactivity, thus facilitating the appearance of SrTiO$_3$ in 10 min of milling.

XRD and FT-IRS data for MA products have also shown that the changes of the components structure and their interaction under milling are more pronounced in the mixtures containing $TiO(OH)_2$ (MA-2 and MA-4) compared to the ones with TiO_2. This difference could be attributed to such factors as the amorphous phase of $TiO(OH)_2$ and a large quantity of OH groups contained in it. It is well known that amorphization of the solid chemicals that can often occur in the course of mechanical treatment increases their reactivity [27–30]. In addition, the interaction during MA is more effective in the mixtures containing hydrated compounds due to the high reactivity of the OH group and the liberation of water increasing the efficiency of energy consumption in comparison with dry milling [29,44,45]. FT-IR spectra for MA-2 and MA-4 (Figure 2) showed a substantial decrease in the intensity of OH–Ti absorbance bands, which could be due to liberation of water from $TiO(OH)_2$ facilitating an acid–base reaction at the interface between acidic $TiO(OH)_2$ and basic $SrCO_3$ or, especially, SrO, which easily formed hydroxide.

2.2. Calcined Samples

2.2.1. Structural Properties

The data on qualitative and quantitative phase composition of MA products annealed at 900 and 1100 °C obtained by the analysis of XRD patterns are presented in Table 1 and Figures 6 and 7. The XRD patterns of MA-1 ($SrCO_3$ + TiO_2) and MA-2 ($SrCO_3$ + $TiO(OH)_2$) calcined at 900 °C (Figure 6) show that they comprise different strontium titanates and the initial $SrCO_3$, but the quantity of each phase in the samples varies significantly. Thus, MA-1 contains comparable amounts of Sr_2TiO_4 [39-1471], $SrTiO_3$ [35-0734] and $SrCO_3$, while for MA-2, the main phase is Sr_2TiO_4 (Table 1 and Figure 6). After annealing at 1100 °C, MA-1 and MA-2 are the single-phase Sr_2TiO_4 (Table 1 and Figure 7). There are no reflections of other phases (SrO or $SrSO_4$) in their XRD pattern but their presence as highly dispersed or surface compounds cannot be excluded. The phase composition of the MA-3 and MA-4 annealed at 900 °C differs considerably. The comparable quantity of $SrTiO_3$ and Sr_2TiO_4 is observed in the case of MA-3 (SrO + TiO_2), while MA-4 (SrO + $TiO(OH)_2$) comprises mainly Sr_2TiO_4. Their phase composition varies little after annealing at 1100 °C (Table 1 and Figure 7).

Table 1. Some characteristics of the samples after annealing of MA products at 900–1200 °C.

Sample/ T °C	Initial Compounds	Phase Composition/ Content,%	Lattice Parameters *, Å			Crystallite size, nm	Specific Surface Area, m²/g
			a	b	c		
MA-1 900 1100	$SrCO_3$ + TiO_2	Sr_2TiO_4 (27.1) $SrTiO_3$ (26.4) $Sr_4Ti_3O_{10}$ (11) $SrCO_3$ (35.5) Sr_2TiO_4 (100)	3.8786	3.8786	12.593	120	3 1.2
MA-2 900 °C 1100 °C	$SrCO_3$ + $TiO(OH)_2$	Sr_2TiO_4 (92.5) $Sr_4Ti_3O_{10}$ $SrTiO_3$ $SrCO_3$ Sr_2TiO_4 (100)	3.8850 3.8756	3.8850 3.8756	12.580 12.561	120 120	1.7 1
MA-3 900 °C 1100 °C	SrO + TiO_2	Sr_2TiO_4 (40) $SrTiO_3$ (57) $Sr_4Ti_3O_{10}$ Sr_2TiO_4 (40) $SrTiO_3$ (56) $Sr_4Ti_3O_{10}$	3.8735 3.9049 3.8856	3.8735 3.8856	12.653 12.647	50	1.9 1.4
MA-4 900 °C 1100 °C	SrO + $TiO(OH)_2$	Sr_2TiO_4 (70) $SrTiO_3$ (14) $Sr_4Ti_3O_{10}$ (16) Sr_2TiO_4 (68) $SrTiO_3$ (14) $Sr_4Ti_3O_{10}$ (18)	3.8861 3.8862	3.8861 3.8862	12.549 12.564	50 120	1.6 1.3

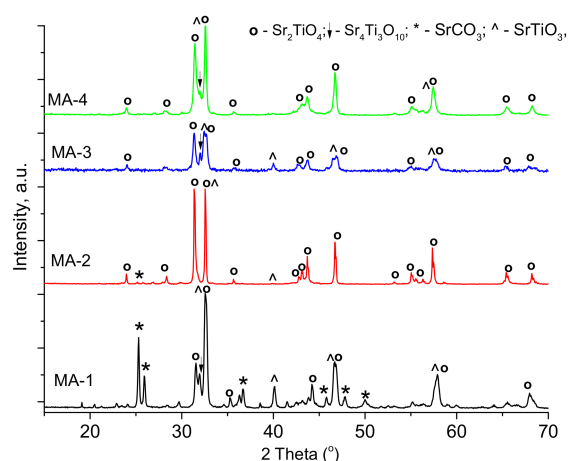* Sr_2TiO_4 [39-1471]: a = b = 3.8861, c = 12.5924.

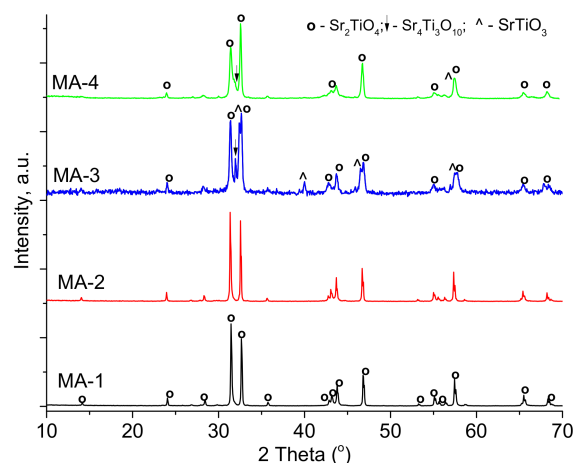**Figure 6.** XRD patterns of the samples annealed at 900 °C.

Figure 7. XRD patterns of the samples annealed at 1100 °C.

As an example, the results of Rietveld refinement for MA-2 (1100 °C) and MA-3 (1100 °C) are presented in Figures 7 and 8. The experimental pattern of MA-2 (1100 °C) and the theoretical one obtained using the known structural data for Sr_2TiO_4 [39-1471] (Figure 7) are qualitatively fit (the reliability factor Rwp = 20.12%), confirming the presence of layered Sr_2TiO_4 of tetragonal structure. The comparison of the experimental pattern for the multiphase MA-3 sample (1100 °C) and the theoretical pattern being superposition of the calculated curves for Sr_2TiO_4, $SrTiO_3$ and $Sr_4Ti_3O_{10}$ is illustrated in Figure 9.

The lattice parameters and the average size of Sr_2TiO_4 crystallites calculated for the samples contained mainly layered perovskite (Table 1). On the whole, the values of the Sr_2TiO_4 lattice parameters are similar and are closer to the ones known in the literature [21,25]. The narrow peaks in the XRD patterns of MA-1, MA-2 and MA-4 calcined at 1100 °C (Figure 7 and Table 1) evidence the presence of the large, well-crystallized particles with a mean size of about 120 nm. In the case of MA-3 (1100 °C), the broader diffraction peaks of perovskite stem from the smaller crystallites of a size of ~50 nm, which could be due to its multiphase composition.
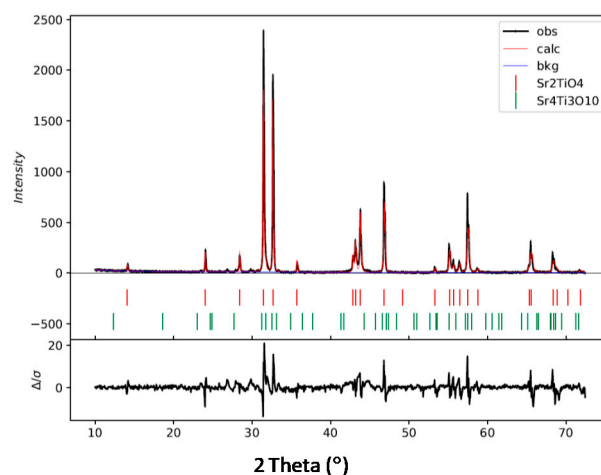
Figure 8. The experimental XRD pattern of MA-2 annealed at 1100 °C (black) and the theoretical one calculated using a model of crystal structure Sr_2TiO_4 [39-1471] (red). The bottom line is the difference plot between observed and calculated values.
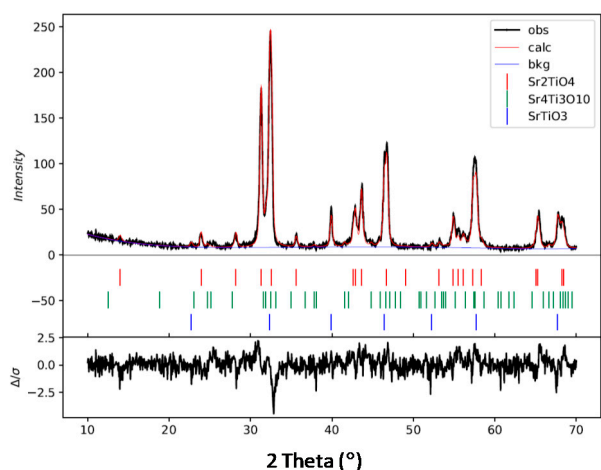

Figure 9. The experimental XRD pattern of MA-3 annealed at 1100 °C (black) and the theoretical one calculated using a model of crystal structure of strontium titanates (red).

Therefore, Sr_2TiO_4, along with other titanates, is formed in all samples after annealing at 900 °C because the interaction of the components in the activated mixtures mainly occurs at the temperatures up to 850–900 °C, was shown for mixtures containing SrO or $SrCO_3$ and TiO_2 [25,26]. However, the phase composition of the samples differs considerably in line with the results for mechanical activation of the corresponding mixtures. Thus, a more pronounced interaction of $SrCO_3$ or SrO with $TiO(OH)_2$ compared to TiO_2 during milling (MA-2, MA-4) leads to the formation mostly of Sr_2TiO_4 after annealing at 900 °C (Table 1 and Figure 6). The MA-1 sample obtained from the mixture of $SrCO_3$ and TiO_2 contains the initial $SrCO_3$, while only titanates are observed in the MA-3 (SrO + TiO_2) sample. Such a difference is due to the lower activity of $SrCO_3$ compared with SrO during activation. Indeed, $SrTiO_3$, being the intermediate in the formation of layered titanates [25,26], is already formed during activation of the mixtures with SrO (Figures 1 and 4).

2.2.2. Surface Composition

The surface composition of the samples calcined at 1100 °C was studied by XPS. The survey spectra of all samples and spectra of Ti $2p_{3/2}$, Sr *3d*, O *1s* are presented in Figures 10 and 11. For all samples, a symmetric Ti $2p_{3/2}$ peak at 457.4–458.1 eV corresponding to the Ti^{4+} in perovskite is observed [46]. All spectra of Sr *3d* show two doublets of

peaks corresponding to Sr^{2+} $3d_{5/2}$ and $3d_{3/2}$ in oxide and perovskite (Figure 10). The peaks related to Sr^{2+} $3d_{5/2}$ are located at 132.2–132.5 eV and 132.7–133.0 eV for the Sr^{2+} in the oxide and perovskite phase, respectively [47–49]. The position of both peaks Sr^{2+} $3d_{5/2}$ (at 132.4 and 132.9 eV) is the same for the single-phase MA-1 and MA-2 annealed at 1100 °C. Some variation in the position of the peaks in the spectra of other samples could be due to their multiphase composition (Table 1), which determines the surface structure features and, as a result, a different charging effect in the position of XPS peaks. O $1s$ spectra show three peaks (Figure 10) corresponding to the oxygen species contained in perovskite (Op) at 529.1–529.4 eV, in oxide or carbonate (O_o) at 531.4–531.6 eV and in hydroxyl groups at 533.8–534 eV [46,47,50]. The low-intensity peak of S $2p$ is also observed for the MA-2 and MA-4 samples prepared using $TiO(OH)_2$ (Figures 10 and 11). The S $2p$ line is barely seen in the spectra of MA-2 and MA-4, which creates difficulties for quantitative analysis by XPS (Figure 10, S $2p$ line). The S/O atomic ratio is ~0.02, so oxygen from sulfate ions is about 8% of the total O $1s$ line intensity, which is close to the XPS error. The binding energy of oxygen from strontium sulfate is 531.8 eV [51], which overlaps with the 531.4 eV peak (Figure 11). Experimental spectra of O $1s$ regions do not allow the addition of extra components in deconvolution that are in agreement with sulfur quantity. At the same time, experimental O $1s$ spectra of MA-2 and MA-4 do not contradict the presence of strontium sulfate.
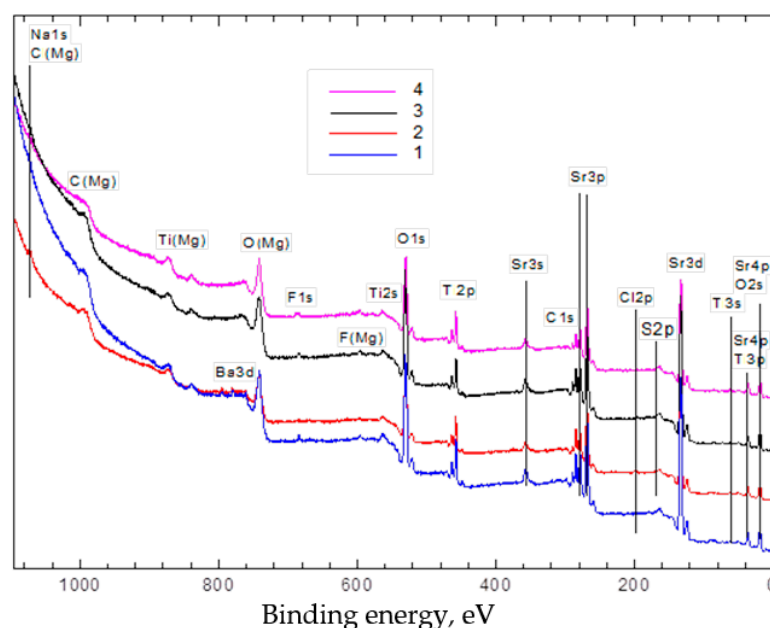

Figure 10. XPS survey spectra. 1—MA-1, 2—MA-2, 3—MA-3, 4—MA-4. F1s is from the set-up pumping system.

The surface composition and concentration of elements calculated using the XPS spectra of the samples are presented in Table 2. XPS analysis shows the presence of sulfur traces in MA-2 ($SrCO_3$ + $TiO(OH)_2$) and MA-4 (SrO + $TiO(OH)_2$) annealed at 1100 °C, which is due to its segregation from the initial $TiO(OH)_2$. The Sr/Ti ratio varies depending on the genesis of the samples. The enrichment of the surface layers with Sr compared with the bulk is observed for all samples, being more marked in the case of MA-1 ($SrCO_3$ + TiO_2) and MA-3 (SrO + TiO_2); the Sr/Ti ratio is equal to 2.5 and 2.9, correspondingly, at the stoichiometric value Sr/Ti = 2. The difference in the Sr/Ti value for MA-1 and MA-3 could result from the phase composition of the samples. Thus, MA-1 consists of the single-phase Sr_2TiO_4, while MA-3 is the multiphase system.
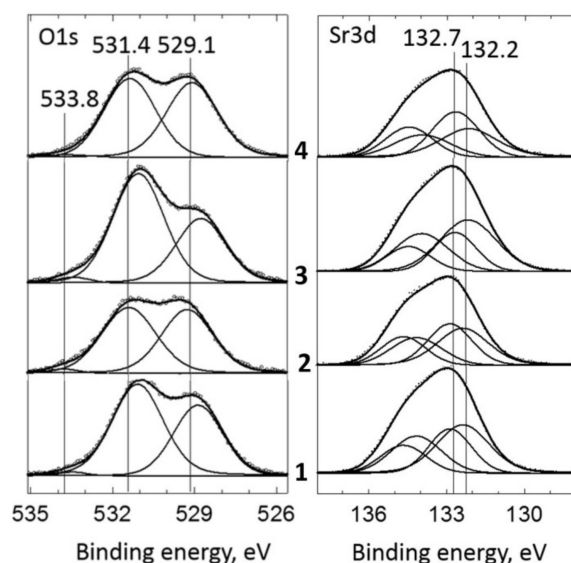
Figure 11. XPS spectra O *1s* and Sr *3d* of the samples calcined at 1100 °C: 1—MA-1, 2—MA-2, 3—MA-3 and 4—MA-4.

Table 2. Atomic ratio of elements in the surface layers and binding energy of oxygen in the different states for the samples calcined at 900–1100 °C obtained from XPS data.

Sample	Sr/Ti	O_p/Ti	O_o/Ti	O_h	O_o/O_p	E_{Op}	E_{Oo}	E_{OOH}
MA-1(1100)	2.5	3.2	4.6	0.086	1.4	529.8	531.1	533.5
MA-2 [1,2](1100)	2.1	3.1	3.3	0.1	1.1	529.2	531.4	533.8
MA-3(1100)	2.9	3.6	6.1	0.2	1.9	528.7	531.0	533.4
MA-4 [1,3](1100)	1.9	3.2	3.2	0.1	1.0	529.1	531.4	533.8

[1]—traces of sulfur; [2,3]—Sr/Ti~1.9 and 1.83 (Sr bulk content); O_o, O_p, O_h,—oxygen in Sr oxide, perovskite and hydroxyl groups, correspondingly.

(Table 1) that can lead to an easier enrichment of the surface with Sr. For MA-2 and MA-4, the smaller value of the Sr/Ti ratio (2.1 and 1.9, respectively) results from some lower Sr content in the samples, as shown by the chemical analysis (Table 2). The values of O_p/Ti equal to 3.1–3.6 show that all samples comprise $SrTiO_3$ as the layers in Sr_2TiO_4 or as the single phase. The high values of the O_o/O_p ratio (1.4 and 1.9) for MA-1 and MA-3 correlate with the Sr enrichment of the surface, evidencing the segregation of SrO. In the case of MA-2 and MA-4, the strontium sulfate formation could be a reason for the smaller O_o/O_p values of 1–1.1 (Table 2).

2.2.3. Textural and Morphological Properties

The specific surface area (SSA) of the calcined samples obtained using the BET method is in the range of 1–3 m^2/g (Table 1). The SSA of the samples annealed at 900 °C is higher for multiphase MA-1 and MA-3 samples, at which the highest SSA was shown by MA-1 (3 m^2/g), including a large amount of $SrCO_3$. By increasing the annealing temperature from 900 to 1100 °C, the value of SSA decreases for all samples. The most marked decline of SSA is observed for MA-1 and MA-2 prepared from the MA products containing $SrCO_3$, which could be a result of its decomposition.

The morphology and the elemental mapping of the samples calcined at 1100 °C were characterized by FE-SEM with EDX. The SEM images show that the form and the size of the particles in the samples depend on their genesis (Figure 12). The typical micrographs of the single-phase MA-1 sample synthesized from the $SrCO_3$ + TiO_2 mixture demonstrate the presence of large, well-crystallized particles with a size of ~500 nm and plates with a thickness of ~50 nm (Figure 12a,b). The micrographs of all other samples show well-crystallized, three-dimensional particles with a size in the range of 200–1000 nm

(Figure 12b–h). For the MA-1 sample, the ordered rows of the light spots of ~10 nm in size are clearly visible on the surface of the plates (Figure 12b), which could be related to the SrO nanospecies in accordance with previous HRTEM data for $Sr_2Ti_{0.9}Mg_{0.1}O_4$ [18]. In the case of MA-2 and MA-4 prepared from the mixtures containing $TiO(OH)_2$, slightly cambered, clear formations are observed. They could be attributed to strontium sulfate, which can be formed on the surface due to decomposition of the sulfate impurity from $TiO(OH)_2$, as XPS data show (Table 2). The elemental maps of Sr and Ti indicate their homogeneous distribution in MA-1 and MA-2 calcined at 1100 °C (Figure 13).
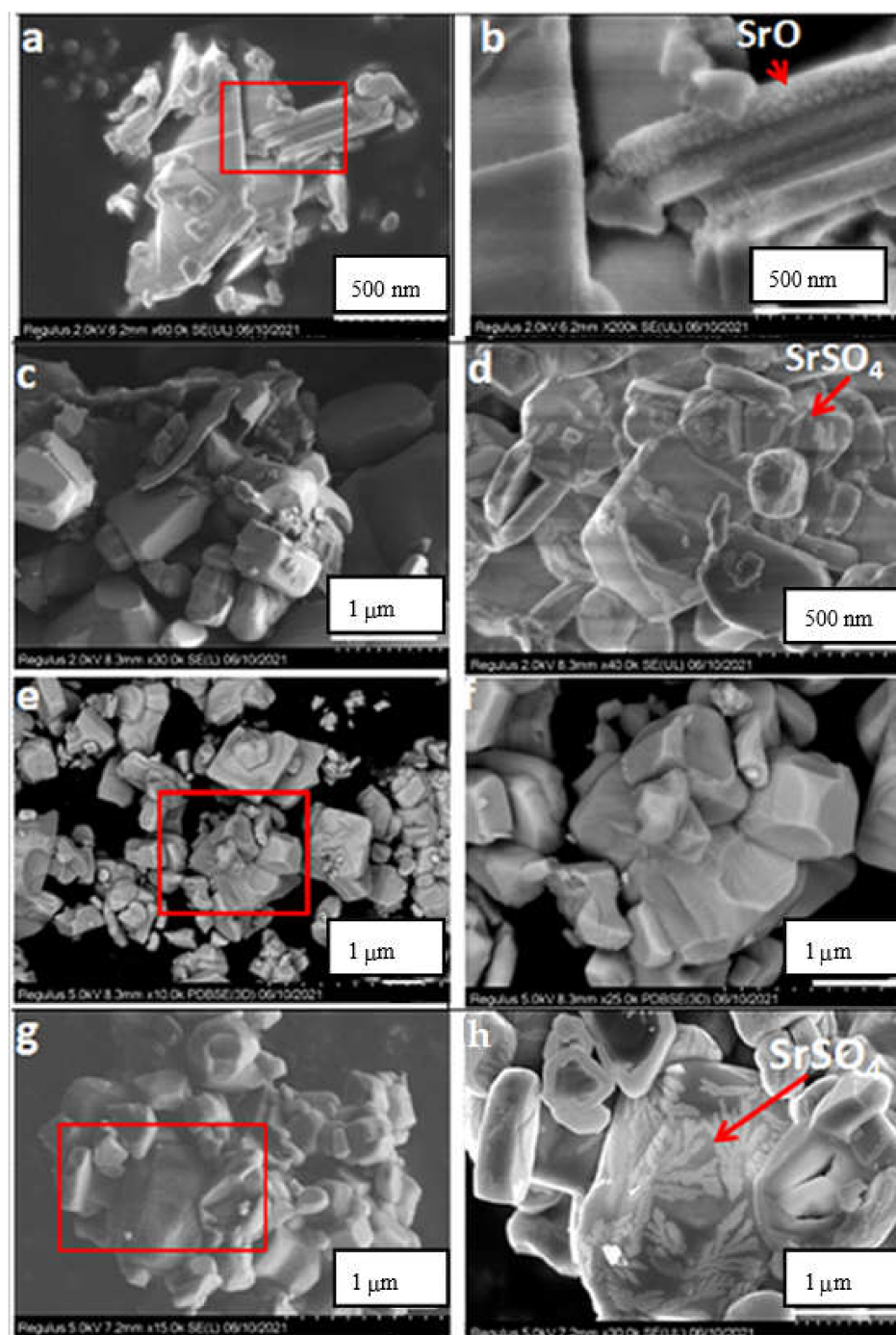

Figure 12. FE-SEM images at different magnifications for the samples calcined at 1100 °C: MA-1 (**a,b**), MA-2 (**c,d**), MA-3 (**e,f**), MA-4 (**g,h**).
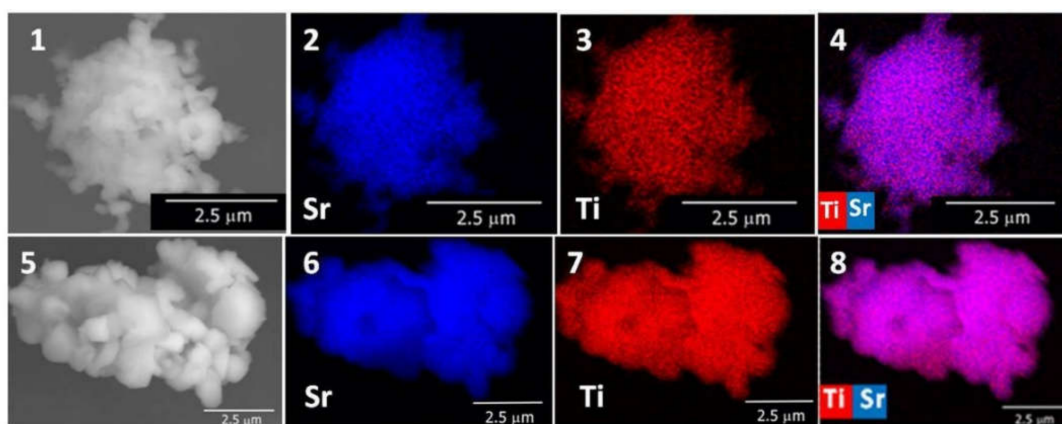
Figure 13. The elemental mapping images of Sr and Ti from the selected area of MA-1 (**1–4**) and MA-2 (**5-8**) annealed at 1100 °C.

2.2.4. Catalytic Activity

The activity characteristics of the samples annealed at 1100 °C in methane oxidative coupling at 800–900 °C are presented in Figure 14. For all samples, methane and oxygen conversion increases, with the temperature rise being maximal at 900 °C, but their values are significantly higher in the case of MA-1 and MA-3, reaching up to 24–25.6% and 82–92%, correspondingly. The activity of the MA-2 and MA-4 catalysts is considerably lower (CH_4 and O_2 conversion of 16–17% and 54–63% at 900 °C, respectively). For the yield of sum C_2 (ethane + ethylene) Y_{C2}, the same trend is observed. Thus, its value of ~15–15.5% is observed for MA-1 and MA-3, while Y_{C2} is only ~9% in the case of MA-2 and MA-4. For all the catalysts, excluding MA-2, the selectivity of C_2 hydrocarbons (S_{C2}) varies with the temperature within 50–63%, being maximal at 850 °C (Figure 14). In the case of MA-2, S_{C2} increases with the temperature rise, reaching ~55% at 900 °C. The selectivity of C_2H_4 grows with the temperature for all catalysts but it is highest In the case of MA-1 and MA-3, reaching up 40 and 37%, respectively. Compared to MA-1 and MA-3, the C_2H_4 selectivity for MA-2 and MA-4 is noticeably lower at 800–850 °C and is close at 900 °C. The ratio of CO/CO_2 selectivities for MA-1 and MA-3 changes with the temperature rise conversely to C_2H_4 selectivity, while it tends to the increase in line with S_{C2H4} for MA-2 and MA-4. Thus, on the whole, the MA-1 and MA-3 samples obtained from MA products of $SrCO_3$ + TiO_2 and SrO + TiO_2 mixtures, correspondingly, are substantially active compared with MA-2 and MA-4 prepared from the mixtures containing $TiO(OH)_2$. This difference could be attributed to the presence of sulfate traces in the surface layers of two latter catalysts (Table 2), blocking methane activation centers and thus reducing their activity. On the whole, the performance of the most active catalysts, MA-1 and MA-3, is comparable with the literature results (Table 3). Note that the analysis and comparison of the catalytic testing data is problematic due to different reaction conditions used. Thus, the most data were obtained at a GHSV of 10,000–18,000 h^{-1}, while our experiments were conducted at a higher GHSV of 75,000 h^{-1}.
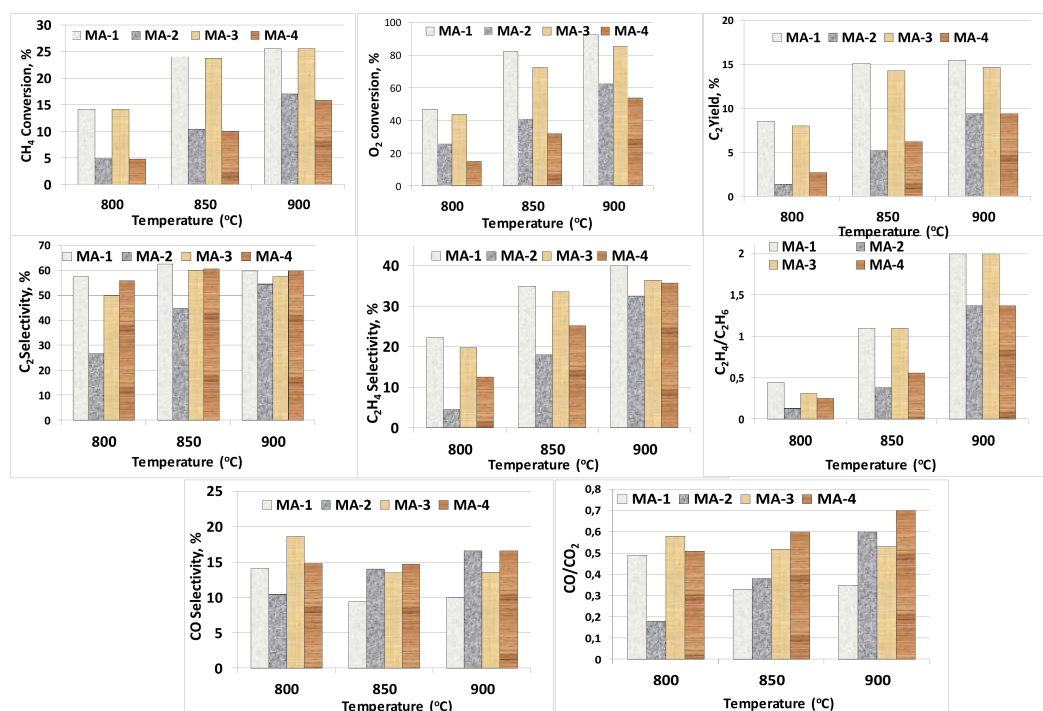
Figure 14. Methane and oxygen conversion, C2 and CO_x selectivity, C2 yield in OCM for the samples annealed at 1100 °C. The reaction mixture—$CH_4:O_2:N_2$ = 46:11.5:42.5% vol., $CH_4:O_2$ = 4, GHSV = 75,000 h^{-1}, 800–900 °C.

Table 3. Some recent studies on the OCM performance of different titanates with a perovskite structure.

Catalyst	Reaction Conditions	Methane Conversion, %	C2 selectivity(S)/ Yield(Y),%	Ref.
$CaTiO_3$ $SrTiO_3$ $BaTiO_3$	700 °C, CH4/O2 = 3, GHSV = 10,000 h^{-1}	13 24 19	2/ 12/ 36/	[16]
$SrTiO_3$ $SrTi_{0.8}Sn_{0.2}O_3$ $SrTi_{0.8}Nd_{0.2}O_3$	800 °C, CH4/O2 = 3, GHSV = 10,000 h^{-1}	32.5 30.8 30.5	48.9/ 52.1/ 54.4/	[52]
$SrZrO_3$	775 °C, CH4/O2 = 3, GHSV = 10,000 h^{-1}	30.7	45.4/	[8]
Sr_2TiO4	850 °C, CH4/O2 = 4, GHSV = 75,000 h^{-1}	19.8	59.6/11.8	[19]
$SrTiO_3$ $Sr_2 TiO_4$ $Sr_2 Ti_{0.9} Mg_{0.1}O4$	850 °C, CH4/O2 = 4, GHSV = 75,000 h^{-1}	-	65.9/12.8 68.5/17.3 71.2/18.2	[18]
Sr_2TiO4 (MA-1) Sr_2TiO4 (MA-3)	850 °C, CH4/O2 = 4, GHSV = 75,000 h^{-1}	24.1	62.7/15.1	This work

OCM is mainly considered to be a heterogeneous–homogeneous process including activation of methane to methyl radicals on the catalyst surface; their subsequent coupling to ethane in the gas phase is then converted into ethylene or CO_x, depending on the peculiarities of the catalyst [1–4]. It is generally implied that formation of methyl radicals by abstraction of hydrogen and oxidative dehydrogenation of ethane to ethylene occur over the active sites if the oxygen species is available on the oxide catalyst surface. Meanwhile, the reagent conversion and product selectivity are affected by the type and concentration of the oxygen species present on the surface. XPS results for all catalysts studied revealed two main types of surface oxygen, corresponding to oxygen in SrO and perovskite $SrTiO_3$

(Table 2). The MA-1 and MA-3 samples demonstrating the most effective performance in OCM show the high ratio of these oxygen forms (O_o/O_p = 1.44 and 1.87) and surface Sr enrichment (Sr/Ti = 2.47 and 2.86, correspondingly). In so doing, the MA-1 sample exhibits some higher oxygen conversion, C_2 selectivity and yield (Figure 14). The presence of Sr cations in the surface layers of the Sr-Ti perovskites are considered to enhance methane conversion and promote C_2 selectivity, especially C_2H_4 [11,14,18]. Bai et al. investigated the effect of the different surface compositions caused by the surface reconstruction of $SrTiO_3$ on its OCM activity [14]. They revealed that in CH_4 conversion, S_{C2} and S_{C2H4} depend on the Sr surface concentration, and they reach maximal values at a certain Sr concentration. It may be assumed that the higher activity of MA-1 compared with MA-3 could be due to an optimal surface concentration of SrO (Sr/Ti = 2.47) and an O_o/O_p ratio equal to 1.44. This difference can result from the different structural and morphological peculiarities of the samples. MA-1 is the single-phase catalyst, while MA-3 is the multiphase one comprising a comparable quantity of $SrTiO_3$ and Sr_2TiO_4. Furthermore, the presence of the plate-like particles with ordered SrO nanospecies on the surface (Figure 12a,b) could contribute to the optimal activity of the surface oxygen and thus to the effective performance of the MA-1 catalyst in OCM. The activity of the multiphase MA-3 catalyst can be attributed to both the surface oxygen of SrO and, possibly, to more weakly bound active oxygen species arising out of the interface boundaries. The latter could be involved in CH_4 partial oxidation that leads to some higher CO selectivity and lower C_2 selectivity for MA-3 compared with the MA-4 catalyst (Figure 14).

The low activity of MA-2 and MA-4 synthesized from mixtures containing $TiO(OH)_2$ is correlated with the low values of the surface Sr concentration (Sr/Ti ~ 2) and O_o/O_p ~ 1 ratio (Table 2). This could be caused by blocking the active oxygen sites with strontium sulfate, which is observed on the surface of the catalysts, as SEM and XPS data shows (Figure 12d,k and Table 2). The methane conversion and sum C_2 yield for both MA-2 and MA-4 are close, while oxygen conversion and C_2 selectivity clearly differs, especially at temperatures below 900 °C: the lower oxygen conversion and the higher C_2 selectivity are observed for MA-4 compared with MA-2 (Figure 14). Such a difference at the close O_o/O_p ratio could be due to the lower surface Sr concentration in the case of MA-4, along with blocking the oxygen active sites to some larger extent compared to MA-2. Thus, the lower CO/CO_2 ratio for MA-2 could suggest the presence of a larger amount of surface oxygen species being active in the deep oxidation of CH_4 to CO_2.

The most active catalysts (MA-1 and MA-3) were tested for 10 h in OCM at 850 °C. The time dependence of the methane conversion and C_2 yield (Figure 15) shows the high long-term stability of the catalyst performance under the highly concentrated reaction mixture and short contact time.

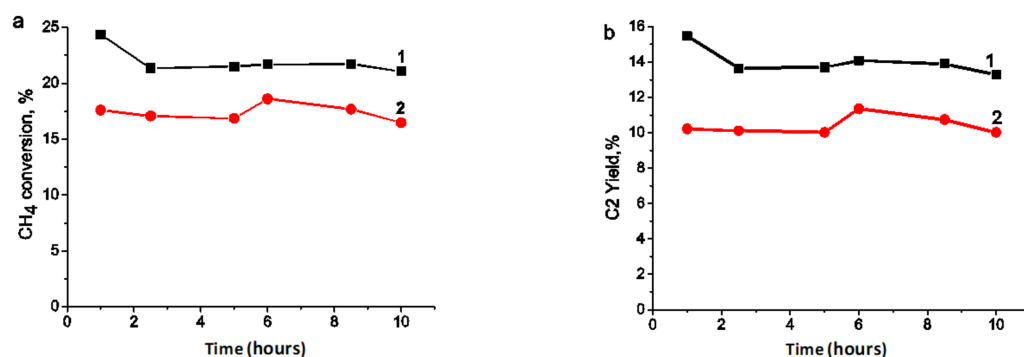**Figure 15.** Time dependence of methane conversion (**a**) and C_2 yield (**b**) in OCM for the MA-1 (1) and MA-3 (2) annealed at 1100 °C. The reaction mixture—CH_4:O_2:N_2 = 46:11.5:42.5% vol., CH_4:O_2 = 4, GHSV = 75,000 h^{-1}, 800–900 °C.

3. Experimental

3.1. Sr$_2$TiO$_4$ Preparation

SrCO$_3$, SrO, TiO$_2$ (rutile) and TiO(OH)$_2$ prepared by hydrolysis of TiOSO$_4$ were used to prepare the Sr$_2$TiO$_4$ samples. SrO was obtained by calcination of Sr(NO$_3$)$_2$ at 900 °C just before the synthesis. To provide a target stoichiometry of samples, corresponding amounts of starting compounds were taken on the basis of their thermal analysis.

The stoichiometric mixtures of the starting chemicals were mixed and then activated in a high-power planetary APF-5 ball mill with two steel drums (25 cm^3 volume) at a 800 rpm rotation rate and an acceleration of 40 g. Mechanochemical activation (MA) of powders was conducted for 10 min under the following conditions: air atmosphere, zirconium balls of 5 mm diameter and a powder-to-ball mass ratio of 1:10. Before each synthesis, a preliminary treatment of drums and balls with the corresponding mixture was performed to cover the surface of the drums and balls by a layer of the initial mixture to minimize contamination of the samples with Fe and Zr due to their rubbing during MA.

Activated mixtures were pressed in tablets and annealed at 900 and 1100 °C.

The composition of the starting mixtures, some characteristics of the samples and their abbreviations are presented in Table 1.

3.2. Catalysts Characterization

Thermal analysis of the starting compounds was carried out with a Q-1500D thermoanalyzer. The phase composition of the samples after MA and annealing were examined by using powder X-ray diffraction (XRD) and IR spectroscopy. XRD patterns were recorded in an X'TRA (Thermo ARL) diffractometer with Cu Ka (λ = 1.5418 Å) radiation in the 2θ angle range 10−70° with a step of 0.05° and an exposure time of 5 s at each step, and graphically processed with the Fityk program. Qualitative phase analysis was carried out by using PDF-2–ICDD files and the ICSD/retrieve database. The quantitative phase analysis was performed through the full pattern simulation method using PCW 2.4 software (http://powdercell-forwindows.software.informer.com/2.4, access date 16 February 2022). The callculated XRD patterns were obtained using the crystal structure database ICSD. To identify the phase structure of the samples, the lattice parameters of the prepared catalysts were obtained by the XRD Rietveld refinement method. FT-IR spectra were recorded in the range of 200–4000 cm^{-1} using a BOMEM MB-102 FT-IR spectrometer.

The specific surface area (S$_{BET}$, m^2/g) was determined by a routine BET procedure using the Ar thermal desorption data. The morphology and elemental mapping of the samples annealed at 1100 °C were studied using a Field Emission Scanning Electron Microscope (FE-SEM) Hitachi Regulus SU8230 equipped with an X-ray microanalysis.

The XPS experiments were performed with a SPECS (Germany) spectrometer equipped with a hemispherical PHOIBOS-150-MCD-9 analyzer. Non-monochromatic MgKα radiation (hν = 1253.6 eV) at 200W was used as the primary excitation. The spectrometer was calibrated using the Au4f$_{7/2}$ (84.0 eV), Ag3d$_{5/2}$ (368.3 eV) and Cu2p$_{3/2}$ (932.7 eV) peaks from metallic gold and copper foils [20]. The binding energies of detected peaks were calibrated by the position of the C1s peak (BE = 284.5 eV). The binding energy values and the areas of XPS peaks were determined after Shirley background subtraction and analysis of the line shapes. The ratios of the surface atomic concentrations of elements were calculated from the integral photoelectron peak intensities corrected by the corresponding relative atomic sensitivity factors based on the Scofield's photo-ionization cross sections and transmission function of the analyzer.

3.3. Activity Tests

The catalytic activity in the OCM reaction was studied in a fixed-bed quartz tube reactor (5 mm inner diameter) at 750–900 °C and ambient pressure. The catalyst (0.2 mL) of 25–50 mesh was diluted with the quartz (1:3) to prevent a temperature gradient in the catalyst bed. The temperature of the catalyst was measured by a chromel–alumel thermocouple placed in the quartz well which was located at the middle of the catalyst bed.

Methane was mixed with air so that the reaction mixture was $CH_4:O_2:N_2 = 46:11.5:42.5\%$ vol., $CH_4:O_2 = 4$. The total feed was 15 L/h corresponding to a gas hourly space velocity (GHSV) of 75,000 h^{-1}. Reactant and product concentrations were analyzed by on-line gas chromatography with Porapack Q (i.d. = 3 mm, l = 3 m) and CaX (i.d. = 3 mm, l = 2 m) columns using a thermal conductivity detector. The reaction products were ethane, ethylene, water, CO, hydrogen and CO_2. Water was removed from the probe with an SiO_2 trap. A blank run with the inert SiO_2 particles (0.25–0.5 mesh) showed no conversion in the reaction conditions.

The methane conversion (X_{CH4}), C_2 selectivity (S_{C2}) and C_2 yield (Y_{C2}) in this study were calculated using the standard normalization method [18], defined as the following equations:

$$X_i = \left(1 - \frac{C_i}{C_i^0}\Delta V\right), \; i = CH_4, O_2,$$

$$S_j = \frac{2C_j}{2C_2H_6 + 2C_{C_2H_4} + 2C_{CO} + 2C_{CO2}}, \; j = C_2H_6, C_2H_4,$$

$$Y_{C_j} = X_{CH_4} \times S_{C_j} \times 100\%,$$

$$S_k = \frac{2C_k}{2C_2H_6 + 2C_{C_2H_4} + 2C_{CO} + 2C_{CO_2}}, \; k = CO, CO_2,$$

$$C - balance = \frac{2C_{C_2H_6} + 2C_{C_2H_4} + 2C_{CO} + 2C_{CO_2}}{C_{CH_4}^0}, \; \Delta V = \frac{C_{N_2}^0}{C_{N_2}},$$

where ΔV is the molar flow rate change, $C_{N_2}^0$, C_{N_2} is the inlet and outlet concentration of N_2, C_i is a component mole fraction. The average carbon balance was not less than 98% in all the tests.

4. Conclusions

The samples of Sr_2TiO_4 were synthesized using mechanochemical activation (MA) of the four mixtures: ($SrCO_3$ + TiO_2), ($SrCO_3$ + $TiO(OH)_2$), (SrO + TiO_2) and (SrO + $TiO(OH)_2$) in a high-energy planetary ball mill, with subsequent annealing at 900 and 1100 °C. XRD and FT-IRS data show that MA for 10 min led to the disordering of the starting component structure in all mixtures and the formation of $SrTiO_3$ only in the case of SrO. These effects were more pronounced in the mixtures with amorphous $TiO(OH)_2$ containing a lot of OH groups.

The XRD Rietveld refinement method showed that, after annealing of the MA products at 900 °C, Sr_2TiO_4 was contained in all samples but its amount was considerably different in line with the peculiarities of MA products. Sr_2TiO_4 was mainly formed in the case of $SrCO_3$ or SrO and $TiO(OH)_2$, in contrast to the mixtures with TiO_2. The single-phase Sr_2TiO_4 is obtained after annealing at 1100 °C only from MA products containing $SrCO_3$.

FE-SEM data demonstrated that the single-phase sample synthesized from the $SrCO_3+TiO_2$ comprised of plates with a thickness of ~50 nm and large, well-crystallized particles with a size of ~500 nm, while all other samples contained only three-dimensional particles of 200–1000 nm. In addition, the presence of the SrO nanospecies of ~10 nm on the plate surface was assumed, while strontium sulfate was probably formed on the surface of the samples prepared using $TiO(OH)_2$ comprised of sulfate impurities.

The surface enrichment with Sr was observed by XPS data in all samples, being more marked in the case of the ones obtained from ($SrCO_3$ + TiO_2) and (SrO + TiO_2): the Sr/Ti ratio was equal to 2.47 and 2.86, correspondingly, at the stoichiometric value Sr/Ti = 2. The testing of the samples in OCM revealed that the CH_4 conversion and C_2 yield correlated with the surface Sr concentration and the ratio of oxygen amount in SrO and perovskite (O_o/O_p). The low activity of the catalysts obtained using $TiO(OH)_2$ could be related to the sulfate formation on the surface after annealing at 1100 °C due to blocking the active sites. The maximal CH_4 conversion and C_2 yield (25.6 and 15.5% at 900 °C, respectively) were observed for the sample obtained from ($SrCO_3$ + TiO_2), showing the specific surface

morphology and optimal values of the surface Sr concentration (Sr/Ti = 2, 47) and a ratio of $O_o/O_p = 1.44$. The most active catalysts (MA-1 and MA-3) showed a high long-term stability performance under the highly concentrated reaction mixture and short contact time.

Author Contributions: S.P.—methodology, conceptualization; Y.I.—validation, investigation; S.T.—investigation; Y.C.—investigation, A.N.—investigation, E.S.—investigation; L.I.—supervision. All authors have read and agreed to the published version of the manuscript.

Data Availability Statement: Informed consent was obtained from all subjects involved in the study.

Conflicts of Interest: The authors declare no conflict of interest.

References

1. Gambo, Y.; Jalil, A.A.; Triwahyono, S.; Abdulrasheed, A.A. Recent advances and future prospect in catalysts for oxidative coupling of methane to ethylene: A review. *J. Ind. Eng. Chem.* **2018**, *59*, 218–229. [CrossRef]
2. Galadima, A.; Muraza, O. Revisiting the oxidative coupling of methane to ethylene in the golden period of shale gas: A review. *J. Ind. Eng. Chem.* **2016**, *37*, 1–13. [CrossRef]
3. Schwach, P.; Pan, X.; Bao, X. Direct Conversion of Methane to Value-Added Chemicals over Heterogeneous Catalysts: Challenges and Prospects. *Chem. Rev.* **2017**, *117*, 8497–8520. [CrossRef] [PubMed]
4. Alexiadis, V.I.; Chaar, M.; van Veen, A.; Muhler, M.; Thybaut, J.W.; Marin, G.B. Quantitative screening of an extended oxidative coupling of methane catalyst library. *Appl. Catal. B Environ.* **2016**, *199*, 252–259. [CrossRef]
5. Kondratenko, E.V.; Schlüter, M.; Baerns, M.; Linke, D.; Holena, M. Developing catalytic materials for the oxidative coupling of methane through statistical analysis of literature data. *Catal. Sci. Technol.* **2015**, *5*, 1668–1677. [CrossRef]
6. Tang, L.; Yamaguchi, D.; Wong, L.; Burke, N.; Chiang, K. The promoting effect of ceria on Li/MgO catalysts for the oxidative coupling of methane. *Catal. Today* **2011**, *178*, 172–180. [CrossRef]
7. Thum, L.; Rudolph, M.; Schomäcker, R.; Wang, Y.; Tarasov, A.; Trunschke, A.; Schlögl, R. Activation in Oxidative Coupling of Methane on Calcium Oxide. *J. Phys. Chem.* **2018**, *123*, 8018–8026. [CrossRef]
8. Sim, Y.; Kwon, D.; An, S.; Ha, J.-M.; Oh, T.-S.; Jung, J.C. Catalytic behavior of ABO3 perovskites in the oxidative coupling of methane. *Mol. Catal.* **2020**, *489*, 110925. [CrossRef]
9. Xu, J.; Xi, R.; Zhang, Z.; Zhang, Y.; Xu, X.; Fang, X.; Wang, X. Promoting the surface active sites of defect BaSnO3 perovskite with BaBr2 for the oxidative coupling of methane. *Catal. Today* **2021**, *374*, 29–37. [CrossRef]
10. Xu, J.; Xi, R.; Xiao, Q.; Xu, X.; Liu, L.; Li, S.; Gong, Y.; Zhang, Z.; Fang, X.; Wang, X. Design of strontium stannate perovskites with different fine structures for the oxidative coupling of methane (OCM): Interpreting the functions of surface oxygen anions, basic sites and the structure–reactivity relationship. *J. Catal.* **2022**, *408*, 465–477. [CrossRef]
11. Ding, W.; Chen, Y.; Fu, X. Influence of surface composition of perovskite-type complex oxides on methane oxidative coupling. *Appl. Catal. A Gen.* **1993**, *104*, 61–75. [CrossRef]
12. Yu, C.Y.; Li, W.Z.; Martin, G.A.; Mirodatos, C. Studies of CaTiO3 based catalysts for the oxidative coupling of methane. *Appl. Catal. A.* **1997**, *158*, 201–214. [CrossRef]
13. Li, X.H.; Fujimoto, K. Low Temperature Oxidative Coupling of Methane by Perovskite Oxide. *Chem. Lett.* **1994**, *23*, 1581–1584. [CrossRef]
14. Bai, L.; Polo-Garzon, F.; Bao, Z.H.; Luo, S.; Moskowitz, B.M.; Tian, H.J.; Wu, Z.L. Impact of Surface Composition of SrTiO3 Catalysts for Oxidative Coupling of Methane. *ChemCatChem* **2019**, *11*, 2107–2117. [CrossRef]
15. Rabuffetti, F.A.; Stair, P.C.; Poeppelmeier, K.R. Synthesis-Dependent Surface Acidity and Structure of SrTiO3 nanoparticles solid-state reaction, molten salt, and sol-precipitation–hydrothermal treatment. *J. Phys. Chem.* **2010**, *114*, 11056–11067. [CrossRef]
16. Lim, S.; Choi, J.-W.; Jin Suh, D.; Lee, U.; Song, K.H.; Ha, J.-M. Low-temperature oxidative coupling of methane using alkaline earth metal oxide-supported perovskites. *Catal. Today* **2020**, *352*, 127–133. [CrossRef]
17. Yang, W.M.; Yan, Q.J.; Fu, X.C. Oxidative coupling of methane over Sr−Ti, Sr−Sn perovskites and corresponding layered perovskites. *React. Kinet. Catal. Lett.* **1995**, *54*, 21–27. [CrossRef]
18. Ivanov, D.V.; Isupova, L.A.; Gerasimov, E.Y.; Dovlitova, L.S.; Glazneva, T.S.; Prosvirin, I.P. Oxidative methane coupling over Mg, Al, Ca, Ba, Pb-promoted SrTiO3 and Sr2TiO4: Influence of surface composition and microstructure. *Appl. Catal. A Gen.* **2014**, *485*, 10–19. [CrossRef]
19. Ivanova, Y.A.; Sutormina, E.F.; Rudina, N.A.; Nartova, A.V.; Isupova, L.A. Effect of preparation route on Sr2TiO4 catalyst for the oxidative coupling of methane. *Catal. Commun.* **2018**, *117*, 43–48. [CrossRef]
20. Ruddlesden, S.N.; Popper, P. New compounds of the K2NIF4 type. *Acta Crystallogr.* **1957**, *10*, 538–539. [CrossRef]
21. Lee, K.H.; Kim, S.W.; Ohta, H.; Koumoto, K. Ruddlesden-Popper phases as thermoelectric oxides: Nb-doped SrO (SrTiO3) (*n* = 1,2). *J. Appl. Phys.* **2006**, *100*, 063717. [CrossRef]

22. Sorkh-Kaman-Zadeh, A.; Dashtbozorg, A. Facile chemical synthesis of nanosize structure of Sr_2TiO_4 for degradation of toxic dyes from aqueous solution. *J. Mol. Liq.* **2016**, *223*, 921–926. [CrossRef]

23. Kwak, B.S.; Do, J.Y.; Park, N.K.; Kang, M. Surface modification of layered perovskite Sr_2TiO_4 for improved CO_2 photoreduction with H_2O to CH_4. *Sci. Rep.* **2017**, *7*, 16370. [CrossRef] [PubMed]

24. Kesić, Ž.; Lukić, I.; Zdujić, M.; Jovalekić, Č.; Veljković, V.; Skala, D. Assessment of $CaTiO_3$, $CaMnO_3$, $CaZrO_3$ and $Ca_2Fe_2O_5$ perovskites as heterogeneous base catalysts for biodiesel synthesis. *Fuel Processing Technol.* **2016**, *143*, 162–168. [CrossRef]

25. Berbenni, V.; Marini, A.; Bruni, G. Effect of mechanical activation on the preparation of $SrTiO_3$ and Sr2TiO4 ceramics from the solid state system $SrCO_3$–TiO_2. *J. Alloy. Compd.* **2001**, *329*, 230–238. [CrossRef]

26. Hungrıa, T.; Hungrıa, A.-B.; Castro, A. Mechanosynthesis and mechanical activation processes to the preparation of the $Sr_2[Sr_{n-1}inO_{3n+1}]$ Ruddlesden–Popper family. *J. Solid State Chem.* **2004**, *177*, 1559–1566. [CrossRef]

27. Fiss, B.G.; Richard, A.J.; Douglas, G.; Kojic, M.; Friščić, T.; Moores, A. Mechanochemical methods for the transfer of electrons and exchange of ions: Inorganic reactivity from nanoparticles to organometallics. *Chem. Soc. Rev.* **2021**, *50*, 8279–8318. [CrossRef]

28. Sepelak, V.; Duvel, A.; Wilkening, M.; Beckerb, K.D.; Heitjans, P. Mechanochemical reactions and syntheses of oxide. *Chem. Soc. Rev.* **2013**, *42*, 7507–7520. [CrossRef]

29. Balaz, P.; Achimovicova, M.; Balaz, M.; Billik, P.; Cherkezova-Zheleva, Z.; Criado, J.M.; Delogu, F.; Dutkova, E.; Gaffet, E.; Gotor, F.J.; et al. Hallmarks of mechanochemistry: From nanoparticles to technology. *Chem. Soc. Rev.* **2013**, *42*, 7571–7639. [CrossRef]

30. Amrute, A.P.; De Bellis, J.; Felderhoff, M.; Schüth, F. Mechanochemical Synthesis of Catalytic Materials. *Chem. Eur. J.* **2021**, *27*, 6819–6847. [CrossRef]

31. Ba-Abbad, M.M.; Kadhum, A.A.H.; Mohamad, A.B.; Takriff, M.S.; Sopian, K. Synthesis and catalytic activity of TiO_2 nanoparticles for photochemical oxidation of concentrated chlorophenols under direct solar radiation. *Int. J. Electrochem. Sci.* **2012**, *7*, 4871–4888.

32. Chen, H.; Chen, D.; Bai, L.; Shu, K. Hydrothermal Synthesis and Electrochemical Properties of TiO_2 Nanotubes as an Anode Material for Lithium Ion Batteries. *J. Electrochem. Sci.* **2018**, *13*, 2118–2125. [CrossRef]

33. Yao, H.; Toan, S.; Huang, L.; Fan, M.; Wang, Y.; Russell, A.G.; Luo, G.; Fe, W. $TiO(OH)_2$—Highly effective catalysts for optimizing CO_2 desorption kinetics reducing CO_2 capture cost: A new pathway. *Sci. Rep.* **2017**, *7*, 2943. [CrossRef] [PubMed]

34. Dutcher, B.; Fan, M.; Leonard, B. Use of multifunctional nanoporous $TiO(OH)_2$ for catalytic $NaHCO_3$ decomposition-eventually for Na_2CO_3/$NaHCO_3$ based CO_2 separation technology. *Sep. Purif. Technol.* **2011**, *80*, 364–374. [CrossRef]

35. Silva, G.M.; Wypych, F. A novel and facile synthesis route for obtaining highly urity free layered hydroxide sulfates: Gordaite and osakaite. *Inorg. Chem. Commun.* **2022**, *143*, 109723. [CrossRef]

36. Asgari-Fard, Z.; Sabet, M.; Salavati-Niasari, M. Synthesis and Characterization of Strontium Carbonate Nanostructures via Simple Hydrothermal Method. *High Temp. Mater. Proc.* **2016**, *35*, 215–220. [CrossRef]

37. Lu, P.; Hu, X.; Li, Y.; Zhang, M.; Liu, X.; He, Y.; Dong, F.; Fub, M.; Zhang, Z. One-step preparation of a novel $SrCO_3$/g-C_3N_4 nano-composite and its application in selective adsorption of crystal violet. *RSC Adv.* **2018**, *8*, 6315–6325. [CrossRef]

38. Márquez-Herrera, A.; Ovando-Medina, V.M.; Castillo-Reyes, B.E.; Zapata-Torres, M.; Meléndez-Lira, M.; González-Castañeda, J. Facile Synthesis of $SrCO_3$-$Sr(OH)_2$/PPy Nanocomposite with Enhanced Photocatalytic Activity under Visible Light. *Materials* **2016**, *9*, 30. [CrossRef]

39. Granados-Correa, F.; Bonifacio-Martínez, J. Combustion synthesis process for the rapid preparation of high-purity SrO powders. *Mater. Sci. -Pol.* **2014**, *32*, 682–687. [CrossRef]

40. Tabah, B.; Nagvenkar, A.P.; Perkas, N.; Gedanken, A. Solar-Heated Sustainable Biodiesel Production from Waste Cooking Oil Using a Sonochemically Deposited SrO Catalyst on Microporous Activated Carbon. *Energy Fuels.* **2017**, *31*, 6228–6239. [CrossRef]

41. Xie, T.; Wang, Y.; Liu, C.; Xu, L. New Insights into Sensitization Mechanism of the Doped Ce (IV) into Strontium Titanate. *Materials* **2018**, *11*, 646. [CrossRef]

42. Grabowska, E.; Marchelek, M.; Klimczuk, T.; Lisowski, W.; Zaleska-Medynska, A. TiO_2/$SrTiO_3$ and $SrTiO_3$ microspheres decorated with Rh, Ru or Pt nanoparticles: Highly UV–vis responsible photoactivity and mechanism. *J. Catal.* **2017**, *350*, 159–173. [CrossRef]

43. Senna, M. A straight way toward phase pure complex oxides. *J. Eur. Cer. Soc.* **2005**, *25*, 1977–1984. [CrossRef]

44. Senna, M. Grinding of mixture under mild condition for mechanochemical complexation. *Int. J. Miner. Processing* **1996**, *187*, 44–45.

45. Avvakumov, E.G.; Karakchiev, L.G. Prospects for soft mechanochemical synthesis. *Chem. Sustain. Dev.* **2014**, *22*, 359–369.

46. Sun, X.; Mi, Y.; Jiao, F.; Xu, X. Activating Layered Perovskite Compound Sr_2TiO_4 via La/N Codoping for Visible Light Photocatalytic Water Splitting. *ACS Catal.* **2018**, *8*, 3209–3221. [CrossRef]

47. Vasquez, R.P. X-ray photoelectron spectroscopy study of Sr and Ba compounds. *J. Electron Spectrosc. Relat. Phenom.* **1991**, *56*, 217. [CrossRef]

48. Pilleux, M.E.; Grahmann, C.R.; Fuenzalida, V.M. Hydrothermal Strontium Titanate Films on Titanium: An XPS and AES Depth-Profiling Study. *J. Am. Ceram. Soc.* **1994**, *77*, 1601–1604. [CrossRef]

49. Wang, K.; Ji, S.; Shi, X.; Tang, J. Autothermal oxidative coupling of methane on the $SrCO_3$/Sm_2O_3 catalysts. *Catal. Commun.* **2009**, *10*, 807–810. [CrossRef]

50. Zhang, W.; Sun, X.; Feifei, B.; He, H. Sol-gel Preparation of Photocatalytic Porous Strontium Titanate using PEG4000 as the Template. *Nanosci. Nanotechnol. -Asia* **2012**, *2*, 183–189. [CrossRef]

51. Vasquez, R.P. $SrSO_4$ by XPS. *Surf. Sci. Spectra* **1992**, *1*, 117. [CrossRef]

52. Lim, S.; Choi, J.W.; Suh, D.J.; Song, K.H.; Ham, H.C.; Ha, J.M. Combined experimental and density functional theory (DFT) studies on the catalyst design for the oxidative coupling of methane. *J. Catal.* **2019**, *375*, 478–492. [CrossRef]